Nanotechnology

PAPER

High performance perovskite solar cells using Cu_9S_5 supraparticles incorporated hole transport layers

To cite this article: Xin Zhou *et al* 2019 *Nanotechnology* **30** 445401

IOP Publishing Nanotechnology
Nanotechnology 30 (2019) 445401 (12pp) https://doi.org/10.1088/1361-6528/ab3604

High performance perovskite solar cells using Cu_9S_5 supraparticles incorporated hole transport layers

Xin Zhou[1], Zaifeng Li[2], Xueshuang Deng[1], Bing Yan[3], Zengbo Wang[3], Xiaohong Chen[1] and Sumei Huang[1]

[1] Engineering Research Center for Nanophotonics & Advanced Instrument, Ministry of Education, School of Physics and Materials Science, East China Normal University, North Zhongshan Rd. 3663, Shanghai 200062, People's Republic of China
[2] College of Civil Engineering, Tongji University, Siping Road 1239, Shanghai 200092, People's Republic of China
[3] School of Electronic Engineering, Bangor University, Bangor LL57 1UT, United Kingdom

E-mail: smhuang@phy.ecnu.edu.cn

Received 15 March 2019, revised 10 July 2019
Accepted for publication 26 July 2019
Published 14 August 2019

Abstract

We disclose novel photovoltaic device physics and present details of device mechanisms by investigating perovskite solar cells (PSCs) incorporating Cu_9S_5@SiO_2 supraparticles (SUPs) into Spiro-OMeTAD based hole transport layers (HTLs). High quality colloidal Cu_9S_5 nanocrystals (NCs) were prepared using a hot-injection approach. Multiple Cu_9S_5 NCs were further embedded in silica to construct a Cu_9S_5@SiO_2 SUP. Cu_9S_5@SiO_2 SUPs were blended into Spiro-OMeTAD based HTLs with different weight ratios. Theoretical and experimental results show that the very strong light scattering or reflecting properties of Cu_9S_5@SiO_2 SUPs blended in the PSC device in a proper proportion distribute to increase the light energy trapped within the device, leading to significant enhancement of light absorption in the active layer. Additionally, the incorporated Cu_9S_5@SiO_2 SUPs can also promote the electrical conductivity and hole-transport capacity of the HTL. Significantly larger conductivity and higher hole injection efficiency were demonstrated in the HTM with the optimal weight ratios of Cu_9S_5@SiO_2 SUPs. As a result, efficient Cu_9S_5 SUPs based PSC devices were obtained with average power conversion efficiency (PCE) of 18.21% at an optimal weight ratio of Cu_9S_5 SUPs. Compared with PSC solar cells without Cu_9S_5@SiO_2 SUPs (of which the average PCE is 14.38%), a remarkable enhancement over 26% in average PCE was achieved. This study provides an innovative approach to efficiently promote the performance of PSC devices by employing optically stable, low-cost and green p-type semiconductor SUPs.

Supplementary material for this article is available online

Keywords: Cu_9S_5 nanocrystal, supraparticle, perovskite solar cell, photovoltaic performance enhancement

(Some figures may appear in colour only in the online journal)

1. Introduction

Perovskite solar cells (PSCs) based on organometal halides have recently emerged as a prominent, efficient and low-cost solar technology. PSC devices originate from a liquid-based dye sensitized solar cells (DSSCs). In this liquid-based DSSC structure, the adsorption of $CH_3NH_3PbI_3$ perovskite on a porous nanocrystalline TiO_2 electrode generates a photocurrent and gains a power conversion efficiency (PCE) of about 3%–4%, as first reported in 2009 [1]. However, the

stability issues of the liquid-based PSC cell are very severe, including immediate disintegration of the perovskite sensitizer in a liquid electrolyte. Stable PSCs with a PCE of about 10% were developed by substituting the liquid electrolyte with a solid hole conductor in 2012 [2–4]. Then, solid-state PSCs have attracted a great deal of attention. Efficiencies have quickly risen from 3.8% [1] to 23.7% [5] in just nine years. Generally, PSCs comprise multiple functional layers and interfaces [3, 6–9]. Comprehending the function and mechanisms of the components in PSC devices can expedite advancements in PSC efficiency and stability [10]. Presently, a lot of academic scientists and researchers are concentrated on promoting the quality of the perovskite active layer and electron transport layer (ETL) using anti-solvent, additive or other novel procedures [11], and mastering their working mechanisms [12]. However, researches into the function of additives in the hole transport layer (HTL) are quite limited [13, 14].

One of the most important advancements for PSC devices in the past several years is the replacement of the liquid electrolyte with the solid-state hole transporting material (HTM) 2,2′,7,7′-tetrakis(*N*,*N*-di-*p*-methoxyphenylamine)-9,9′-spirobifluorene (Spiro-OMeTAD). This substitution dramatically improves the stability and the efficiency of PSCs [3, 15]. In spite of the benefits that it brings to PSCs, the pristine uncharged form of Spiro-OMeTAD suffers from intrinsic low hole mobility and low conductivity. Effective strategies are needed to solve the inherent shortages, such as adding dopants. Actually, Spiro-OMeTAD is the generally used HTM in solid-state dye sensitized solar cells (SDSSCs). During the development of the SDSSC technology, chemical p-dopants like $N(PhBr)_3SbCl_6$ were introduced to oxidize and dope Spiro-OMeTAD for the first time. Shortly afterwards, it were substituted with bis(trifluoromethane)sulfonimide lithium salt (LiTFSI) and 4-tert-butylpyridine (tBP) [16–18]. LiTFSI is the p-dopant, and tBP is the additive that acts as a recombination blocking agent. This combination was initially employed to SDSSCs, and extensively utilized to PSCs to date [19]. In addition, Cobalt dopants and perfluoro-tetracyanoquinodimethane F_4TCNQ have also been exploited to enhance the hole conductivity of Spiro-OMeTAD [20, 21]. Therefore, additives play an important part in promoting the hole conductivity of the Spiro-OMeTAD film and eventually raise the efficiency of PSCs.

Copper sulfides with a formula of $Cu_{2-x}S$ ($0 \leqslant x < 1$) have been widely investigated as plasmonic semiconductors. They are intrinsic hole-conducting (p-type) and direct band semiconductors, and their bandgap is in the range of 1.2–2.5 eV, depending on the specific phase and stoichiometry. $Cu_{2-x}S$ is a low-cost, environmentally benign and nontoxic material [22, 23]. Moreover, the nonstoichiometric copper sulfide nanocrystals (NCs) display near-infrared (NIR) localized surface plasmonic resonance (LSPR) absorption from excessive holes in the valence band due to the presence of copper vacancies, which endows them with the ability to fundamentally tailor light–matter interactions and potential applications in bio-imaging [24], photothermal therapy [25] and optical devices [26]. Zhang *et al* reported a molecular precursor solution method to prepare Cu_9S_5 thin film as the back electrode of a CdTe solar cell [27]. Lei *et al* assembled PSCs based on a doped Spiro-OMeTAD/$Cu_{7.5}S$ double layered HTM by vacuum thermal evaporation of CuS powders, reaching a PCE of 17.91% [28]. Very recently, Han *et al* fabricated a planar PSC with an undoped Spiro-OMeTAD/Cu_9S_5 double layered HTM and nitrogen doped SnO_2 ETL, achieving a maximum PCE of 17.10% [29]. Cu_9S_5 was proven to be a superior HTL and electrode interface modification layer in both polymer and PSC solar cells [29, 30]. It shows a splendid electrical conductivity, high mobility of copper ions, high work function and a suitable energy level alignment with the perovskite absorber. Copper chalcogenide nanomaterials are still in their initial PSC application stages, which have a humongous measure of space for further advancement. The efficiency of the PSCs can be promoted by the insertion of Cu_9S_5, an inorganic material, to construct a high quality organic and inorganic hybrid HTL. Additionally, as well known, the light–matter interaction in noble metal (gold and silver) nanostructures has extensively studied in order to improve photon absorption and thus improve the photon-to electron conversion efficiency of photovoltaic (PV) devices [31]. Through rational designs, surface plasmon resonance of plasmonic semiconductor nanostructures could also help to enhance the solar energy harvesting by different mechanisms involving plasmon-enhanced solar light harvesting, hot carrier injection, resonant energy transfer, near-field enhancement and scattering (far -field effect) [32–35]. Cu_9S_5 NCs in a suitable configuration hybridized with organic HTM can be expected to optically engineer the PSC device to maximize light coupling/trapping into the photoactive layer due to their unique optical natures, including LSPR and scattering effects in the NIR range as well as low dissipation in the visible wavelength [36].

In this work, for the first time to our knowledge, $Cu_9S_5@SiO_2$ supraparticles (SUPs) are employed in HTLs to improve the PV performance of PSCs. High quality colloidal Cu_9S_5 nanocrystals (NCs) were synthesized via a hot-injection method. Multiple Cu_9S_5 NCs were further embedded in silica to form a $Cu_9S_5@SiO_2$ SUP. The synthesized $Cu_9S_5@SiO_2$ SUPs were incorporated in Spiro-OMeTAD based HTLs with different weight ratios. The weight ratio of $Cu_9S_5@SiO_2$ UPs has a great impact on the PV performance of the PSC device. It was found that with the addition of the Cu_9S_5 SUPs in a proper proportion, the composite HTL exhibited higher conductivity, charge carrier transfer/collection ability and greater hole injection efficiency. Additionally, the embedded SUPs also functioned as light scattering or reflecting centers to boost the light intake of the PSCs. At the optimal weight ratio of Cu_9S_5 SUPs, the average PCE of 18.21% was obtained for the $Cu_9S_5@SiO_2$ SUPs based PSC devices under one sun (AM1.5 G) illumination. Compared with PSC solar cells without $Cu_9S_5@SiO_2$ SUPs (of which the average PCE is 14.38%), a remarkable enhancement over 26% in average PCE was obtained. The basic optics and physics behind the PSC devices based on $Cu_9S_5@SiO_2$ SUPs was investigated.

2. Experimental detail

2.1. Synthesis of Cu_9S_5 NCs

The Cu_9S_5 NCs were synthesized via a typical hot injection method [36]. The copper precursor was prepared by mingling CuCl (0.01 mol) with a mixture of 4 ml of oleic acid (OA) and 5 ml of oleylamine (OM) at 130 °C for 30 min. Then the as-prepared copper precursor was cooled to room temperature. Meanwhile, the sulfur precursor was prepared by dissolving sulfur powders (0.01 mol) in 40 ml of octadecene at 200 °C for 30 min. And the sulfur solution was maintained at 180 °C, followed by swift injection of the copper precursor. Before cooling to the room temperature, the resulting solution was kept at 180 °C for 10 min Cu_9S_5 NCs in the solution were precipitated by adding excess acetone and collected by centrifugation of the suspension for two times. Finally, the precipitate was re-dispersed in an organic solvent such as cyclohexane.

2.2. Synthesis of Cu_9S_5@SiO_2 SUPs

Cu_9S_5@SiO_2 SUPs were synthesized via a modified Stöber's method [37], namely by the ammonia-catalyzed hydrolysis and condensation of tetraethylorthosilicate (TEOS) in alcohol solution. In brief, the as-prepared Cu_9S_5 NCs (0.2 g), 10 ml of cyclohexane, 0.5 ml ammonia, 10 ml Triton X-100, 8 ml hexyl alcohol, 2 ml water and 0.1 ml TEOS were successively added under stirring. After completion of TEOS addition, the mixture was allowed to react for 24 h, after which the products were collected and washed for three times with alcohol.

2.3. Device fabrication

Fluorine-doped tin oxide (FTO) coated slides (Pilkington TEC 15) were patterned by etching with Zn powders and 2 M HCl. Then, the etched slides were cleaned with liquid detergent, acetone, ethyl alcohol and de-ionized water for 15 min, sequentially, to remove the organic or inorganic residues, and finally dried in a vacuum oven. Isopropyl titanate (222 μl) and ethanol (5 ml) were blended to prepare a clear precursor sol. The precursor sol was spin-coated onto the etched FTO substrate at 4000 rpm, followed by annealing at 500 °C for 30 min to form a compact TiO_2 (c-TiO_2) film. A mesoporous TiO_2 (mp-TiO_2) film was deposited on the c-TiO_2 by spin-coating TiO_2 paste (Dyesol 18NR-T) diluted in anhydrous ethanol (weight ratio: 1:6) at 4000 rpm for 30 s. The layers were then sintered at 500 °C for 30 min in air. After cooling down to the room temperature, the samples were treated using a $TiCl_4$ aqueous solution at 70 °C for 30 min, and dried at 500 °C for 30 min.

A pure perovskite solution (1.25 mol l^{-1}) was made by blending CH_3NH_3I (0.2963 g) and PbI_2 (0.8678 g) powders in γ-butyrolactone (GBL) (1.05 ml) and dimethylsulfoxide (DMSO) (0.45 ml) at 60 °C for 6 h. Subsequently, the perovskite solution was then spin-coated onto the mp-TiO_2 layer by a one-step process at 4000 rpm for 50 s to form the perovskite absorber film. Anhydrous ether was dripped onto the center of the sample at 30 s during the spin-coating process. Then, the perovskite sample was heated at 110 °C for 30 min [11, 38]. 72.3 mg of Spiro-OMeTAD, 28.8 μl of 4-tert-butyl pyridine (TBP) and 17.5 μl of Li-TFSI in acetonitrile (520 mg ml^{-1}) were dissolved in 1 ml chlorobenzene to form a Spiro-MeOTAD solution. After the perovskite film samples were cooled down to room temperature, the formed Spiro-MeOTAD solution was deposited on the perovskite layer at 4000 rpm for 30 s. To prepare Cu_9S_5@SiO_2 SUP modified HTLs, the Spiro-OMeTAD solution was mixed with the prepared chlorobenzene solution of Cu_9S_5 NCs or Cu_9S_5@SiO_2 SUPs. The used weight ratio of Cu_9S_5@SiO_2 SUPs to Spiro-OMeTAD was 0.4 wt%, 0.6 wt%, 0.8 wt%, 1 wt% and 1.2 wt%, respectively. Finally, a 100 nm thick AgAl film with an active area of 0.1 cm^2 was formed via evaporation on the Spiro-OMeTAD-coated film [39, 40].

2.4. Characterization of samples

The optical reflectance spectra and light absorption nature of the perovskite films were examined and characterized by a Hitachi U-3900 UV–vis spectrophotometer. The light absorption properties of the Cu_9S_5 NCs were determined via UV–vis–NIR light absorption spectroscopy (Lambda 950, PerkinElmer). The transmission electron microscope (TEM) images were recorded on a Hitachi H-800 TEM under a working voltage of 200 kV. The cross sectional view of the formed PSC device was examined by emission scanning electron microscopy (SEM) on a JEOL-2010F (JEOL Co. Ltd). X-ray diffraction (XRD) was performed using a Bruker New D8 Advance with a Cu-Kα radiation source (λ: 1.5406 A) at 40 kV and 300 mA (12 kW). The photocurrent density–voltage (J–V) curves were recorded via a Keithley model 2440 Source Meter under the illumination of simulated AM 1.5 G solar light from a Newport solar simulator system (equipped with a 1 kW Xenon arc lamp, Oriel, calibrated with a standard silicon reference cell). During device PV performance characterization, a metal aperture mask with an opening of about 0.09 cm^2 was employed. External quantum efficiency (EQE) measurements (74125, Oriel, USA) were recorded for these cells. The time-resolved PL (TRPL) spectra were collected by picosecond time-correlated single-photon counting (TCSPC) equipment. The detailed information about this picosecond TCSPC equipment is described in the [41].

3. Results and discussion

The process of fabricating Cu_9S_5@SiO_2 SUPs and the structure of Cu_9S_5@SiO_2 SUP based PSCs are displayed in Scheme 1. At the beginning, Cu_9S_5 nanospheres were grown via a hot-injection method [36]. The formed Cu_9S_5 nanospheres were mono-dispersed and homogeneous, with a diameter (d) of about 10 nm, as shown in figure 1(a). Cu_9S_5 nanocrystals were further inlaid in SiO_2 via the modified Stöber's approach [37], producing Cu_9S_5@SiO_2 SUPs with a diameter of about 60 nm (figures 1(b) and (c)).

The XRD patterns of the obtained Cu_9S_5 NCs and Cu_9S_5@SiO_2 SUPs match well with the standard pattern of

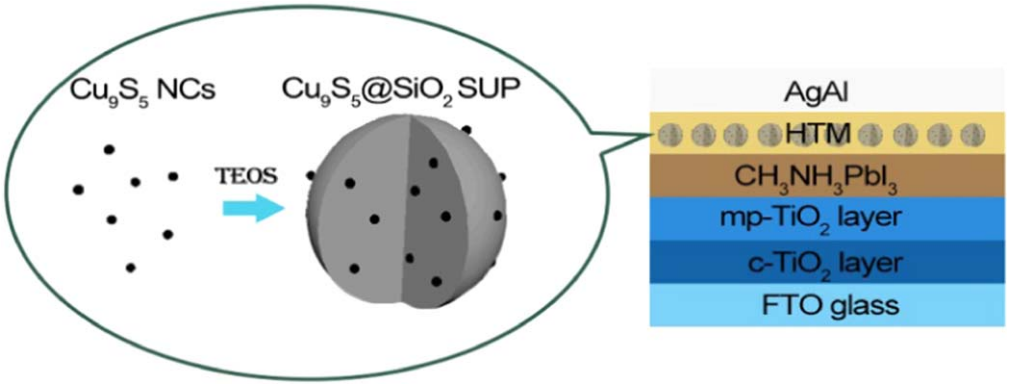

Scheme 1. Fabrication process of Cu_9S_5@SiO_2 supraparticles (SUPs) and application in PSCs.

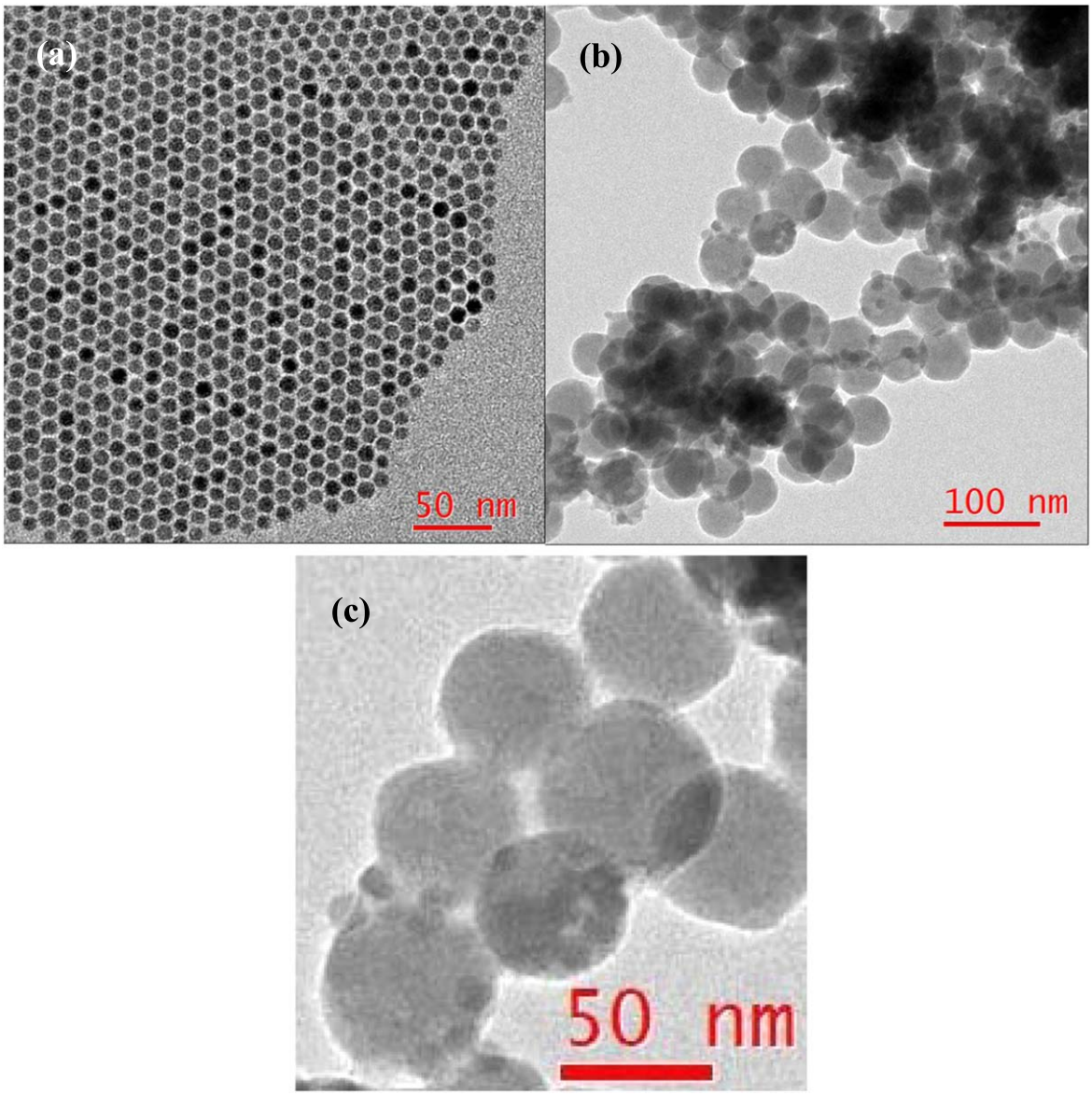

Figure 1. TEM image of (a) Cu_9S_5 nanocrystals, (b) and (c) Cu_9S_5@SiO_2 supraparticles.

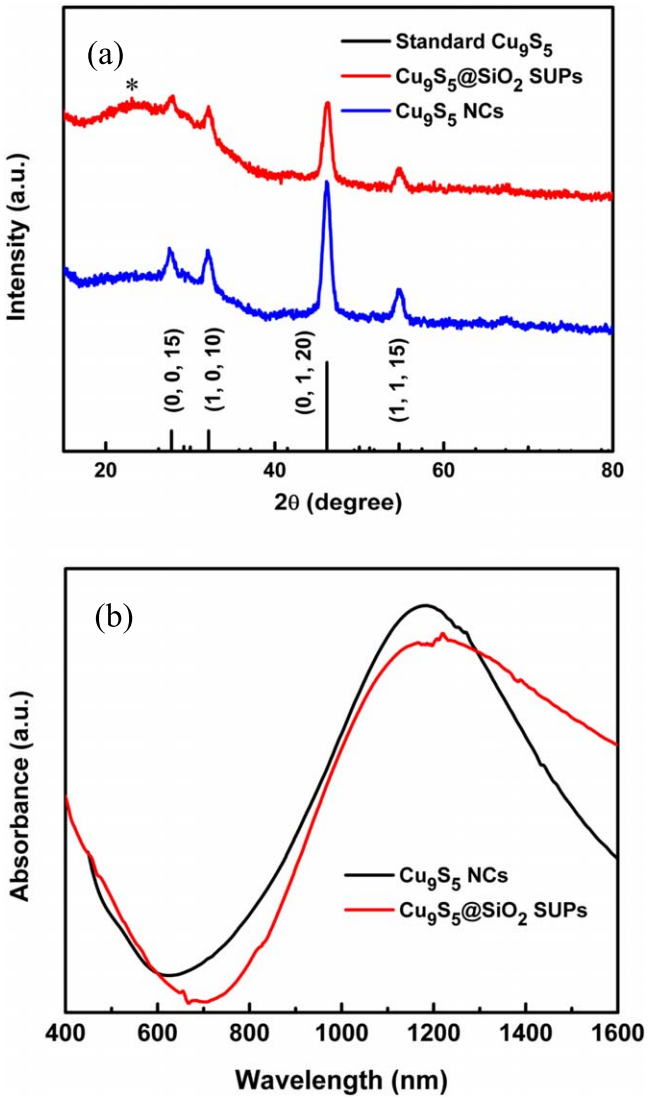

Figure 2. (a) XRD patterns of the as-prepared Cu_9S_5 NCs, Cu_9S_5@SiO_2 SUPs and the standard Cu_9S_5 powders on a JCPDS card (no. 47-1748). (b) UV–vis–NIR absorption spectra of Cu_9S_5 NCs and Cu_9S_5@SiO_2 SUPs.

Cu_9S_5 digenite phase (JCPDS no. 47-1748), as presented in figure 2(a). Several well—defined characteristic peaks corresponding to the (0, 0, 15), (1, 0, 10), (0, 1, 20) and (1, 1, 15) crystal planes specify the formation of pure rhombohedral phase of Cu_9S_5 with high crystallinity. Moreover, for the Cu_9S_5@SiO_2 SUP sample, the wide and weak peak centered at $2\theta = 23°$ reveals the amorphous structured silica coating within such composites [42]. The optical property of the aqueous dispersion containing Cu_9S_5 nanocrystals and Cu_9S_5@SiO_2 SUPs was examined by using UV–vis–NIR spectroscopy, as shown in figure 2(b). Cu_9S_5 nanocrystals clearly show a wide surface plasmon absorption band over the visible and near infrared regions centered at 1240 nm. Compared to the case of Cu_9S_5 NCs, the plasmon resonance peak of Cu_9S_5@SiO_2 SUPs displays an apparent redshift and a slight decrease in the intensity, caused by the silica coating [43, 44]. The localized surface plasmon resonance (LSPR) of Cu_9S_5 nanoparticles derives from collective oscillations of excess free carriers associated with constitutional vacancies or ionized dopant impurities in the lattice, which is different from the free electron induced LSPR of metal nanostructures [45].

In order to evaluate the PV performance of the device employing Cu_9S_5@SiO_2 SUPs to engineer HTM films, three types of HTLs were employed, including Spiro-OMeTAD (control) without and with Cu_9S_5@SiO_2 SUPs or Cu_9S_5 NCs. The amount of Cu_9S_5@SiO_2 SUPs in Spiro-OMeTAD precursor solution was controlled as 0.4, 0.6, 0.8, 1 and 1.2 wt%, respectively, and the proportion of Cu_9S_5 NCs was 0.8 wt%. The cross-section SEM image of as-prepared PSCs is displayed in figure 3(a), from which we can confirm the layered structure of the PSC device. The photocurrent density–voltage curves (J–V) of the PSCs measured under one sun illumination at AM 1.5 G are shown in figure 3(b). The corresponding average PV parameters and the dependence on Cu_9S_5@SiO_2 SUP or Cu_9S_5 NC concentrations have been determined and the results are summarized in table 1. As can be seen from figure 3(a) and table 1, the control device without modification reveals an average short-circuit current density (J_{SC}) 21.24 mA cm^{-2}, a mean open-circuit voltage (V_{OC}) 1.01 V, an average fill factor (FF) of 67.06% and PCE of 14.38%. The corresponding cells based on a low content of 0.4 wt% $Cu_{2-x}S$@SiO_2 SUPs induced a higher V_{OC} and J_{SC}, resulting in a slightly enhanced average PCE of 14.78%. Employing Cu_9S_5@SiO_2 SUPs as additive to HTLs, a simultaneous enhancement in V_{OC}, J_{SC} and FF can be observed as the amount of Cu_9S_5@SiO_2 SUPs is increased from 0.4 wt% to 0.8 wt%. Specifically, the V_{OC} increases from 1.01 to 1.05 V, the J_{SC} increases from 22.24 to 23.14 mA cm^{-2}, and most distinctly the FF increases from 65.16% to over 74.95%. As a consequence, the devices obtained from the Spiro-OMeTAD solution with 0.8 wt% Cu_9S_5@SiO_2 SUPs provided average efficiencies of 18.21%. In solar cells, the FF was reported to principally be associated with the series resistance (R_S) and shunt resistance (R_{SH}) [46, 47], which can be estimated from the J–V results. The increased FF is in well coincident with the decreased R_S and increased R_{SH} which can be seen from table 1. The lowest R_S and highest R_{SH} is in well coincident with the largest FF for the PSC based on 0.8 wt% Cu_9S_5@SiO_2 SUPs. However, a further increase in the amount of Cu_9S_5@SiO_2 SUPs from 0.8 wt% to 1.0 wt%, or even 1.2 wt% leads to a dramatically reduced V_{OC}, FF and PCE. Besides, Cu_9S_5 nanocrystals were also incorporate into HTLs. The PV performance of the PSC devices without modification and with 0.8 wt% Cu_9S_5 NCs or 0.8 wt% Cu_9S_5@SiO_2 SUPs was more clearly compared and shown in figure 3(c). As can be seen from table 1, the device based on 0.8 wt% Cu_9S_5 NCs exhibits an average J_{SC} of 22.43 mA cm^{-2}, V_{OC} of 1.05 V, FF of 72.40% and PCE of 17.05%. These PV parameter values are higher than those of the control, nevertheless, obviously lower than those of the PSC bases on Cu_9S_5@SiO_2 SUPs. The approach by incorporating Cu_9S_5@SiO_2 SUPs into HTLs at the optimal weight ratio of 0.8 wt% significantly boosts the average PCE to 18.21%. Figure 3(d) shows the EQE spectra of the PSC devices without modification and with 0.8 wt% Cu_9S_5 NCs or

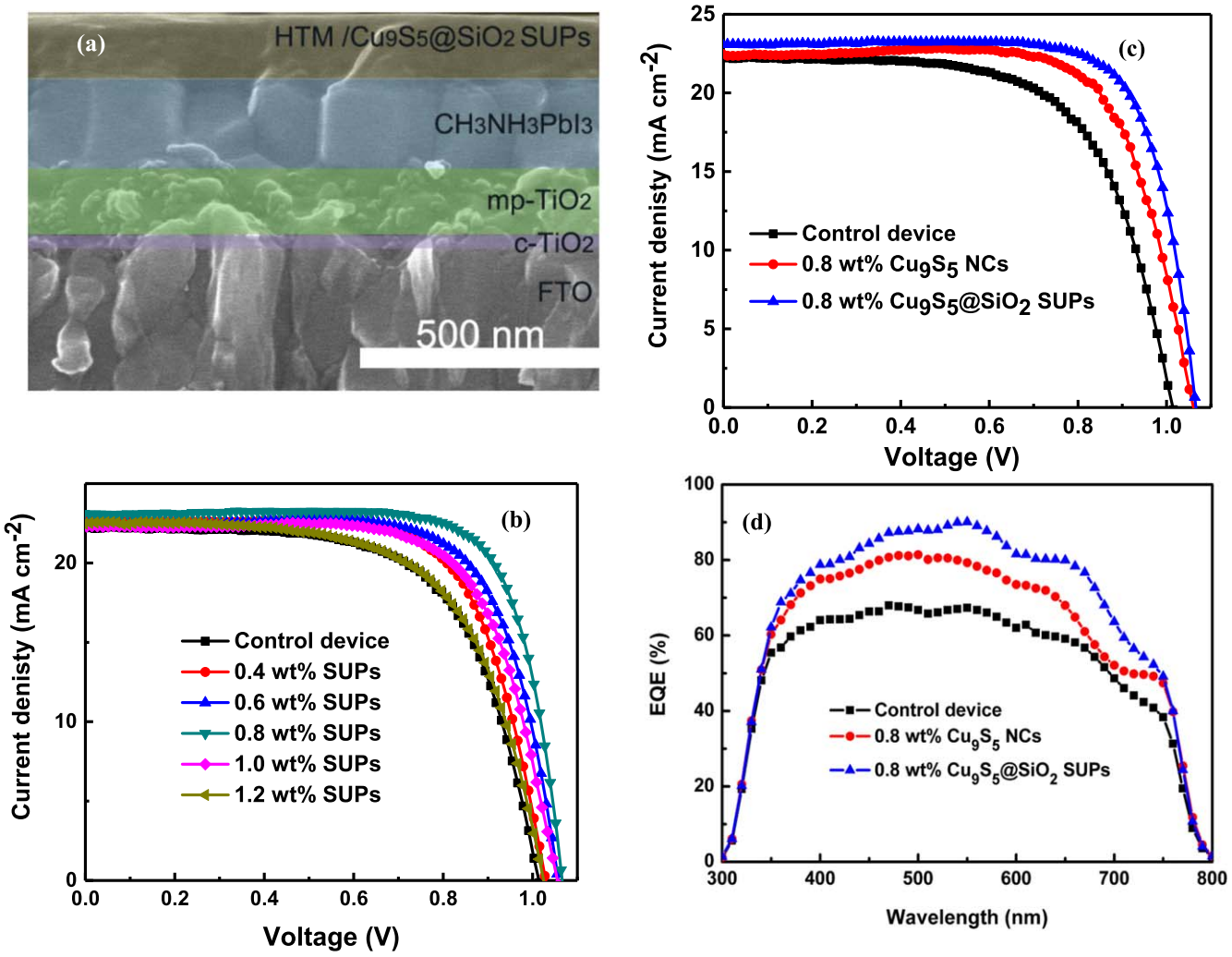

Figure 3. (a) Cross-sectional SEM image of Cu_9S_5@SiO_2 supraparticle based PSCs. (b) *J*–*V* characteristics of PSC devices with different amounts of Cu_9S_5@SiO_2 supraparticles. (c) *J*–*V* characteristics and (d) EQE spectra of the control device, and PSCs with 0.8 wt% Cu_9S_5 NCs or 0.8 wt% Cu_9S_5@SiO_2 supraparticles.

Table 1. Photovoltaic parameters of PSCs using hybrid HTLs with various ratios of Cu_9S_5@SiO_2 supraparticles or Cu_9S_5 nanocrystals.

Sample (wt%)	V_{OC} (V)	J_{SC} (mA cm^{-2})	FF (%)	PCE (%)	R_S (Ω cm^2)	R_{SH} (Ω cm^2)
Control device	1.01 ± 0.01	21.24 ± 1.02	67.06 ± 3.06	14.38 ± 0.16	81	42 503
0.4 wt% SUPs	1.02 ± 0.02	21.96 ± 0.71	69.58 ± 0.61	15.66 ± 0.52	82	59 906
0.6 wt% SUPs	1.02 ± 0.02	22.50 ± 0.35	70.23 ± 1.62	16.12 ± 0.84	57	70 377
0.8 wt% SUPs	1.05 ± 0.02	23.14 ± 0.10	74.95 ± 0.72	18.21 ± 0.61	44	136 448
1.0 wt% SUPs	1.02 ± 0.01	22.67 ± 0.09	70.62 ± 1.07	16.42 ± 0.23	71	102 485
1.2 wt% SUPs	1.01 ± 0.01	22.11 ± 0.40	64.49 ± 0.67	14.49 ± 0.13	101	47 519
0.8 wt% Cu_9S_5 NCs	1.05 ± 0.01	22.43 ± 0.41	72.40 ± 1.46	17.06 ± 0.34	55	80 446

0.8 wt% Cu_9S_5@SiO_2 SUPs as a function of the wavelength. The generation of photocurrent starts at ~800 nm for all three devices. Thus, the spectral response of the PSCs are limited to the wavelength range of 300–800 nm, which is far away from to the absorption peak of Cu_9S_5 nanomaterials shown in figure 2(b), implying that the solar light harvesting enhancement induced by LSPRs of Cu_9S_5 nanostructures is finite in $CH_3NH_3PbI_3$ based PSCs. From figure 3(d), within the wavelength range from 400 to 750 nm, the photocurrent increased remarkably after incorporating Cu_9S_5 NCs and Cu_9S_5@SiO_2 SUPs compared to the control device, especially for the case of Cu_9S_5@SiO_2 SUPs, which is in good agreement with the J_{SC} extracted from the corresponding *J*–*V* curve shown in figure 3(c). Moreover, the EQE spectrum of the PSC device based on 0.8 wt% Cu_9S_5@SiO_2 SUPs exhibits significantly higher quantum yields over a wide wavelength scope from 350 to 750 nm with a maximal value of 91%. When employing Cu_9S_5 NCs or Cu_9S_5@SiO_2 SUPs as

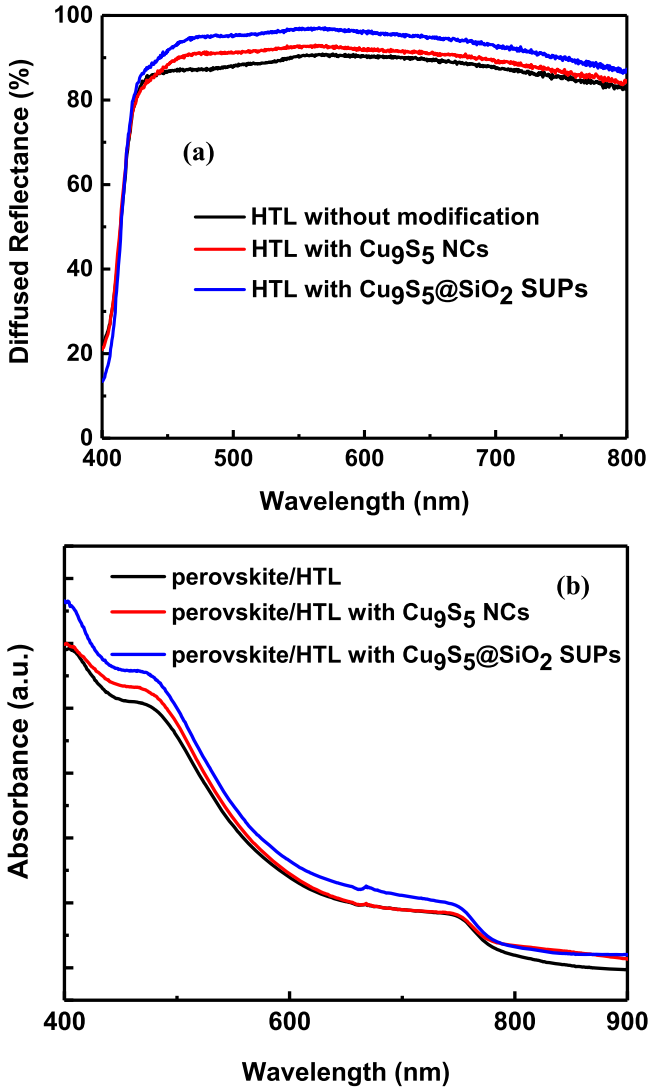

Figure 4. (a) Diffused reflectance spectra of glass/FTO/ bare HTL/AgAl and glass/FTO/ HTL@0.8 wt% Cu_9S_5 NCs or Cu_9S_5@SiO_2 SUPs/AgAl samples. (b) UV–vis absorption spectra of glass/$CH_3NH_3PbI_3$/bare HTL and glass/$CH_3NH_3PbI_3$/HTL@0.8 wt% Cu_9S_5 NCs or Cu_9S_5@SiO_2 SUPs samples.

additive to HTLs, the increase in V_{OC}, J_{SC}, FF or EQE values may be ascribed to the improved scattering and electronic properties of HTLs by addition of these Cu_9S_5 based nanomaterials. The corresponding discussion will be made in the subsequent sections.

To understand the underlying optical mechanism of the PV performance enhancement in the Cu_9S_5@SiO_2 SUPs incorporated PSC device, the optical natures of HTL/AgAl and perovskite/HTL hybrid layers, the important component parts for PSC devices, were probed. Figure 4(a) displays the diffused reflectance spectra of glass/FTO/bare HTL/AgAl and glass/FTO/HTL containing 0.8 wt% Cu_9S_5

NCs or Cu_9S_5@SiO_2 SUPs/AgAl samples. The light scattering (reflection) of the composite HTL-back metal electrode sample slightly but clearly increases by the addition of Cu_9S_5 NCs, and considerably increases by the incorporation of Cu_9S_5@SiO_2 SUPs in the optical region from 450 to 800 nm. These results undoubtedly suggest that the Cu_9S_5 NCs or Cu_9S_5@SiO_2 SUPs act as scattering centers and increase the light path inside the PSC device. The tremendously strengthened reflectance in the Cu_9S_5@SiO_2 SUP modified HTL/AgAl sample definitely confirm the more effective light scattering or reflecting of Cu_9S_5@SiO_2 SUPs than Cu_9S_5 NCs both in the visible and NIR regime. The more effective light scattering or reflecting of Cu_9S_5@SiO_2 SUPs could extend both visible and NIR light path-lengths within the perovskite active layer and thus efficiently boost solar light harvesting in the PSC device. Figure 4(b) displays the UV–vis absorption spectra of hybrid samples consisted of glass/$CH_3NH_3PbI_3$/HTL without modification and with Cu_9S_5 NCs or Cu_9S_5@SiO_2 SUPs modification. The sample of glass/$CH_3NH_3PbI_3$/HTL containing Cu_9S_5 NCs or Cu_9S_5@SiO_2 SUPs shows more intense absorption over 400–900 nm than the control sample without modification, due to the scattering or reflecting effect of Cu_9S_5 NCs and SUPs. It is noted that the absorbance of the perovskite composite sample is most dramatically enhanced over 400–900 nm with the addition of Cu_9S_5@SiO_2 SUPs, as expected from the reflectance results shown in figure 4(a). The absorption results for perovskite composite samples based on differently structured HTLs are in good agreement with those from *J*–*V* and EQE measurements shown in figures 3(c) and (d). When sunlight is incident on the PSC, the light transmitting through the glass and the FTO layer was absorbed by the perovskite layer. The unabsorbed light energy, especially for long-wavelength light, was reflected back into the perovskite absorber by the Cu_9S_5 NCs, the Cu_9S_5@SiO_2 SUPs or the back AgAl electrode and absorbed again by the perovskite to generate extra charge carriers, leading to an enhancement in the performance of the PSCs shown in table 1 and figure 3. Therefore, the intense efficiency enhancement in the PSC device by addition of Cu_9S_5@SiO_2 SUPs can be at least partially associated with the relatively effectively scattering or reflecting effect of Cu_9S_5@SiO_2 SUPs.

On the other hand, using the EQE and absorption measurement data shown in figures 3(d) and 4(b), we further calculate the increase percentage in EQE ($\Delta EQE/EQE_{ref}$) and absorption ($\Delta Abs/Abs_{ref}$) with the addition of Cu_9S_5 NCs or Cu_9S_5@SiO_2 SUPs, which we show in figure S1 (available online in the supplementary information stacks.iop.org/NANO/30/445401/mmedia). From the figure, the EQE enhancement is broadly distributed over the wide range from 350 to 750 nm with a maximal value at 650 nm for the PSC based on Cu_9S_5@SiO_2 SUPs and does not specifically follow the plasmon mode profile shown in figure 2(b). Moreover, for the case modified with Cu_9S_5 NCs or Cu_9S_5@SiO_2 SUPs, the enhancement percentage obtained from the light absorption of the perovskite composite sample is much lower than that of the EQE incremental quantity over the wavelength range of 400–650 nm, where the spectral response of the solar cell is high. When the wavelength is near and beyond the edge of the absorption band of perovskite film, the sharply increased absorption enhancement could be attributed to the quick increase absorption of the Cu_9S_5 nanomaterials. The broad

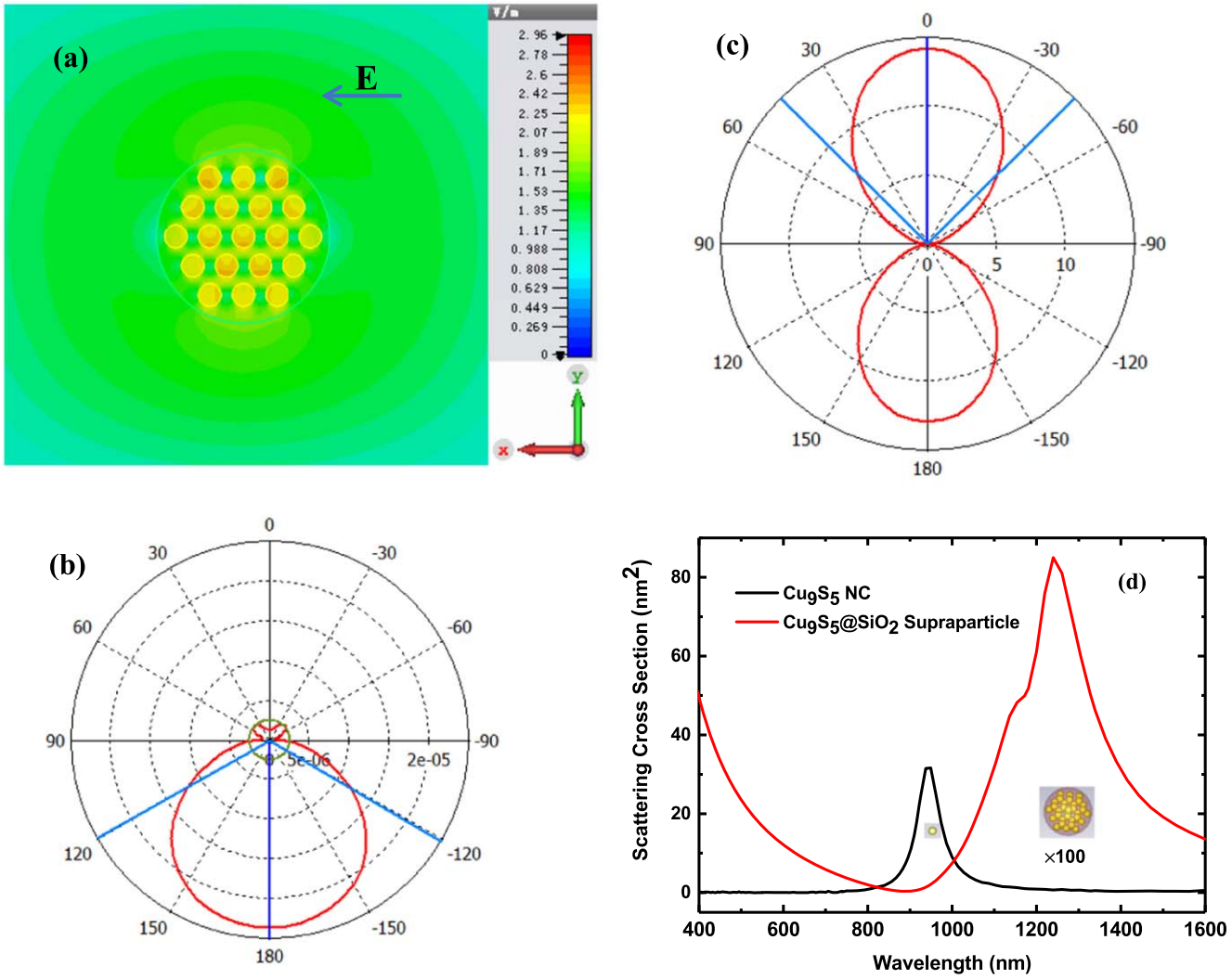

Figure 5. (a) Simulated field $|E|$ enhancement distribution of 60 nm Cu_9S_5@SiO_2 supraparticle in the HTM. Scattering diagrams for a (b) 10 nm Cu_9S_5 nanosphere and a (c) 60 nm Cu_9S_5@SiO_2 supraparticle illuminated by a linear polarized plane wave in free space. (d) Calculated scattering cross sections of 10 nm Cu_9S_5 nanocrystal and 60 nm Cu_9S_5@SiO_2 supraparticle.

and intense EQE enhancement in the high spectral response range of the device suggests that the enhanced device performance of Cu_9S_5 NC or SUP composite PSCs mainly come from semiconductor plasmonically enhanced electrical properties of the Cu_9S_5 composite HTL, rather than from optical effects alone [7, 8, 31].

Light incident on semiconductor nanoparticles can be scattered into the far-field, depending on geometric and material properties of the particle [48, 49]. Finite-difference time-domain (FDTD) numerical simulations were performed for spherical Cu_9S_5 NC and Cu_9S_5@SiO_2 SUP. The computation was based on the finite integral technique (CST Microwave Studio) [7, 8, 49]. The optical properties (refractive index, n, and extinction coefficient, *k*) of the related materials are from the data in previous publications [36, 50–52]. FDTD numerical simulations were performed for a Cu_9S_5@SiO_2 spherical SUP embedded in HTM. The center of the Cu_9S_5@SiO_2 SUP located at the origin. Figure 5(a) shows the calculated local amplitude enhancement distribution of the electric field $|E|$ in the *xy* plane for an incident light at $\lambda = 550$ nm, where the maximal absolute EQE value was obtained. From figure 5(a), the electric field is enhanced and localized inside or around the Cu_9S_5 crystals or Cu_9S_5@SiO_2 SUP, and the maximum $|E|$ enhancement factor is about 2.4. The near field enhancement can be a result of coupling between individual plasmonic Cu_9S_5 particles and the interaction between Cu_9S_5@SiO_2 SUPs and HTM in close proximity [53]. When semiconductor NPs in a SUP are very adjacent to each other, higher-order interactions and even energy transfer may occur.

Figure 5(b) and (c) show angular scattering diagrams for a 10 nm Cu_9S_5 nanoparticle and 60 nm Cu_9S_5@SiO_2 SUP illuminated by a linear polarized plane wave with a wavelength (λ) of 550 nm in free space. An angle of 0° correlates with backward scattering while 180° correlates with forward scattering. The Cu_9S_5 nanoparticles scatter more radiation in the forward direction than in the backward direction (figure 5(b)). In contrast, for the Cu_9S_5@SiO_2 spherical SUP, the far-field angular distribution pattern becomes more backscattering (figure 5(c)). These results are consistent with prior

research [31, 54]. In the case of spherical nanoparticles, relatively smaller particles are known to result in more scattering in the forward direction while larger particles scatter more in the backward direction (as a reflection).

Figure 5(d) shows the calculated scattering cross-sections of spherical Cu_9S_5 nanoparticle and $Cu_9S_5@SiO_2$ SUP in free space. Multiple Cu_9S_5 nanoparticles with a small size were assemble into a nanocapsule with a large size using silica to form a $Cu_9S_5@SiO_2$ SUP. The scattering efficiency of $Cu_9S_5@SiO_2$ SUP peaks at 1240 nm due to the surface plasmon resonance of multiplex Cu_9S_5 NPs, as shown in figure 2(b). Moreover, the $Cu_9S_5@SiO_2$ SUP has tremendously stronger scattering properties than the Cu_9S_5 nanoparticle. The scattering cross section of the former is two orders of magnitude larger than that of the latter. This result strongly support the much more effectively scattering or reflecting effect of $Cu_9S_5@SiO_2$ SUPs blended in HTL/AgAl of the PSC device. This far-field scattered light can ultimately be reabsorbed by the perovskite semiconductor, enabling enhanced light absorption, photocurrent and thus, PCE in $Cu_9S_5@SiO_2$ SUPs based PSCs.

Cu_9S_5 is a good hole-conducting inorganic material, which can be applied as the back electrode for CdTe solar cells [27]. For a $Cu_9S_5@SiO_2$ SUP, multiple Cu_9S_5 NCs are in close proximity to each other, and encapsulated by SiO_2. At the same time, some Cu_9S_5 NCs are left exposed on the surface of the SUP, as shown in figure 1(c). $Cu_9S_5@SiO_2$ SUPs allow the combination of multiple Cu_9S_5 NCs into a single entity. Such SUPs not only carry on the good electrical conductivity and hole-transport capacity of its constituent building blocks, i.e. Cu_9S_5 NCs, but may reveal additional functional properties, hence surpassing the sum of its parts. Higher-order interactions and even tunneling may take place between the Cu_9S_5 NCs in the SUPs [50]. Therefore, in addition to the function as scattering or reflecting center to increase the total light energy trapped within the PSCs, doping of $Cu_9S_5@SiO_2$ SUPs can also improve the electrical conductivity and hole-transport capacity of HTL. In order to carry out the related tests, the precursor HTM solutions without modification and modified with 0.8 wt% Cu_9S_5 NCs or $Cu_9S_5@SiO_2$ SUPs were directly deposited on FTO slides to prepare HTLs, and subsequently, 100 nm thick AgAl film was evaporated on the grown HTLs. The structure of the multi-layered device is exhibited in the inset of figure S3. *J–V* characteristics of the multi-layered device were measured by applying a bias between the AgAl electrodes on the HTM and the FTO layers and under dark conditions, as shown in figure S3. The conductivity of the spiro-MeOTAD based HTL with and without modification can be simulated from *J–V* characteristics of this two-contact electrical conductivity set-up [18]. The value we obtain for the conductivity in pure spiro-MeOTAD is 1.74×10^{-6} S cm^{-1}, in very good agreement with that reported in [55]. The conductivity increases with the addition of 0.8 wt% Cu_9S_5 NCs or $Cu_9S_5@SiO_2$ SUPs, exhibiting 3.64×10^{-6} Scm^{-1} and 4.09×10^{-6} S cm^{-1}, respectively. Encouragingly, when the small amount of $Cu_9S_5@SiO_2$ SUPs is added, the conductivity increases by 2.3 times. The result substantiates that the introduction of the $Cu_9S_5@SiO_2$ SUPs remarkably enhances the conductivity of HTL and is well-matched with the improved performance of PSCs mentioned in the previous sections.

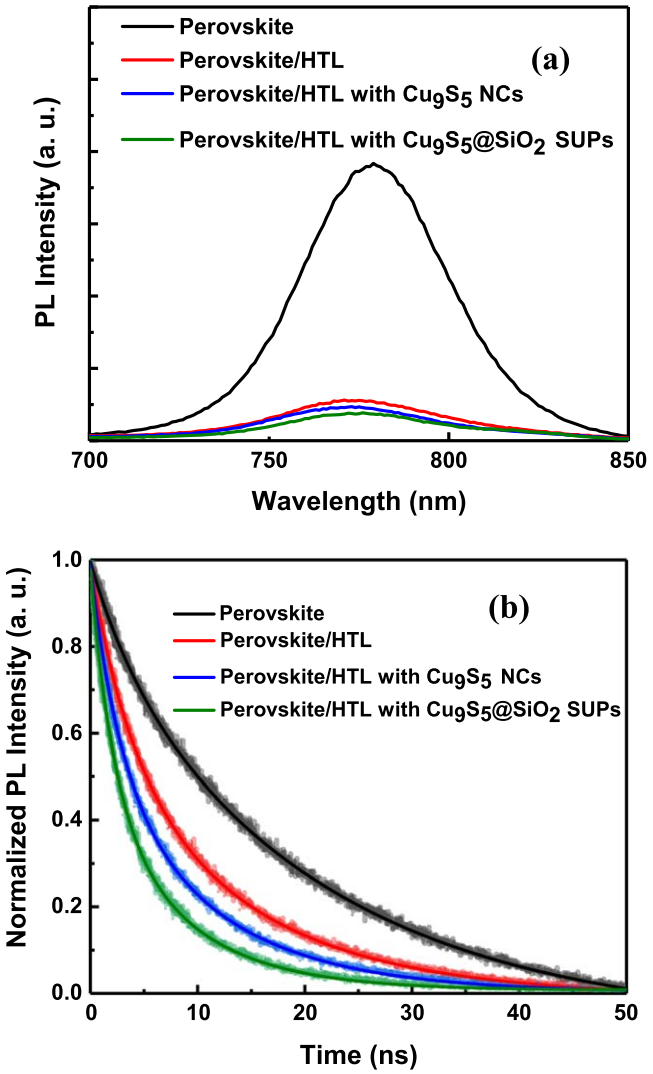

Figure 6. Steady-state PL spectra (a) and time-resolved PL decays (b) of samples consisting of glass/$CH_3NH_3PbI_3$ and glass/$CH_3NH_3PbI_3$/HTL without modification and with 0.8 wt% Cu_9S_5 NCs and 0.8 wt% $Cu_9S_5@SiO_2$ SUPs.

To investigate the charge transfer process at the perovskite and Cu_9S_5 NCs, $Cu_9S_5@SiO_2$ SUPs modified HTL interface, steady-state photoluminescence (PL) and TRPL decay transient spectra were recorded for the $CH_3NH_3PbI_3$/HTL samples prepared on glass substrates. As can be seen from figure 6(a), the bare perovskite film shows a strong emission peak at about 760 nm, and the PL is significantly quenched when the bare Spiro-OMeTAD HTL is applied onto the perovskite film, indicating that efficient charge carrier transfer at the perovskite/HTL interface. When the Cu_9S_5 NCs and $Cu_9S_5@SiO_2$ SUPs incorporated HTL is used, the PL quenching is even more intensely, especially for the case of the $Cu_9S_5@SiO_2$ SUPs modified HTL. Quenching effects clearly indicated that the introduction of $Cu_9S_5@SiO_2$ SUP into the HTL facilitated charge transfer and separation at the perovskite/HTL interface. The $CH_3NH_3PbI_3$/HTL

Table 2. Summarized fitting parameters taken from the time-resolved PL curves in figure 6(b) by two exponential decay functions and average PL decay lifetimes (τ_{av}), PL rate constants (k_{PL}), injection rate constants (k_{inj}), and injection efficiencies (Φ_{inj}) of different samples.

Sample	A_1	τ_1 (ns)	A_2	τ_2 (ns)	τ_{av} (ns)	k_{PL} (s^{-1})	k_{inj} (s^{-1})	Φ_{inj} (%)
Perovskite	12.43%	3.93	87.57%	21.26	20.81	4.8×10^7	—	—
Perovskite/HTL	38.19%	3.76	61.81%	13.74	12.29	8.1×10^7	3.3×10^7	40.74
Perovskite/HTL @Cu_9S_5 NCs	44.66%	2.71	55.34%	10.74	9.38	1.1×10^8	6.2×10^7	56.36
Perovskite/HTL @Cu_9S_5 SUPs	48.89%	2.11	51.11%	8.04	6.85	1.5×10^8	1.0×10^8	66.67

containing Cu_9S_5@SiO_2 SUPs sample exhibits the lowest PL peak intensity and the strongest degree of PL quenching. The most intense PL quenching suggests the rapidest charge transfer, the most effective hole extraction and the lowest recombination rate, and hence likely the highest short-circuit current, FF and the best PV performance [55, 56]. These results are further supported by the TRPL measurements shown in figure 6(b). The PL lifetimes of these bilayer samples were characterized by monitoring the peak emission at 760 nm. The TRPL spectra can provide an insight into the photo-physical properties of PSCs, including the charge accumulation at perovskite/HTL interface and the charge transfer or charge separation/injection behavior [57, 58]. The PL decay spectra can be well-fitted using a two-exponential equation, yielding a fast decay characterized by the lifetime, τ_1, together with a slow component, τ_2. It is known that the fast decay process reflects the charge carrier capturing by defects and the radiative decay process, and the slow decay process is mainly associated with the charge carrier transfer process across the interface [59]. Therefore, in this paper, slow decay times are utilized to comparison. The pristine perovskite film displays the largest PL lifetime with τ_2 of 21.26 ns. The PL lifetime is significantly shortened when Spiro-OMeTAD layer is coated onto perovskite film. The corresponding τ_2 value for the case of the bare HTL is 13.74 ns. When the Cu_9S_5 NCs are doped into HTL, the formed perovskite/HTL with Cu_9S_5 NCs displays faster decay with a τ_2 of 10.74 ns. It can be noticed that when the HTL is doped with Cu_9S_5@SiO_2 SUPs, the device exhibits the fastest decay with a τ_2 of 8.04 ns. This can be attributed to the efficient charge carrier transfer and high hole mobility induced by the incorporation of Cu_9S_5@SiO_2 SUPs. Both the steady-state and TRPL decay results matched well. There is no doubt that the Cu_9S_5@SiO_2 SUPs based PSCs exhibited the highest J_{SC}, V_{OC}, and FF values for all of the devices tested here, clearly suggesting the better hole-collection ability with the addition of Cu_9S_5@SiO_2 SUPs into Spiro-OMeTAD. The results show a definite effect of p-doping in improving the charge carrier transport/extraction of the HTL.

The average PL decay time (τ_{av}) was calculated by the following equation (1): [60]

$$\tau_{av} = \frac{\sum A_i \tau_i^2}{\sum A_i \tau_i}. \quad (1)$$

The value of τ_{av} of different device was shown in table 2. The hole injection efficiency, Φ_{inj}, can be expressed by equation (2):

$$\Phi_{inj} = k_{inj}/(k_{inj} + k_o). \quad (2)$$

Here the injection constant (k_{inj}) is defined as $k_{inj} = k_{HTL} - k_o$, where k_{HTL} and k_o is the PL rate constant determined from the PL lifetimes of the perovskite film with different types of HTL and single perovskite film, respectively. In general, these rate constants can be expressed by the inverse of the monitored emission lifetimes, τ_{av}, which was determined by TRPL measurement [61, 62]. The specific data is shown in the table 2. For the unmodified HTL sample, the hole injection efficiency is 40.74%. When Cu_9S_5 NCs are incorporated into HTL, the hole injection efficiency increases to 56.36%. When Cu_9S_5@SiO_2 SUPs are added into HTL, the hole efficiency increases up to 66.67%. This result further demonstrates the addition of Cu_9S_5@SiO_2 SUPs leads to significant enhanced hole injection from perovskite film to HTL.

4. Conclusions

We have developed efficient PSCs by embedding Cu_9S_5@SiO_2 SUPs into Spiro-OMeTAD based HTLs. High quality and mono-disperse Cu_9S_5 NCs were synthesized using a hot-injection approach. Cu_9S_5@SiO_2 SUPs were form by embedding numerous Cu_9S_5 NCs in silica. Cu_9S_5@SiO_2 SUPs were added into Spiro-OMeTAD based HTLs with different weight ratios. The contribution of the optical and electrical effects of Cu_9S_5@SiO_2 SUPs to the PV performance improvement has been investigated through theoretical modeling and experiment. Both theoretical and experimental studies show that the intense light scattering or reflecting natures of Cu_9S_5@SiO_2 SUPs embedded in the PSC device in a suitable proportion donates to boost the light energy trapped within the device, resulting in clearly enhanced light absorption in the active layer. In addition, the incorporated Cu_9S_5@SiO_2 SUPs remarkably improve the electrical conductivity and hole-transport characteristics of the HTL. With using Cu_9S_5@SiO_2 SUPs at the optimal ratio, the conductivity and the hole injection efficiency in the HTM were 2.3 and 1.6 times higher than those of the pure Spiro-OMeTAD HTL without modification. Consequently, the incorporation of an optimized ratio Cu_9S_5@SiO_2 SUPs in PSC devices promotes the average PCE from 14.38% to 18.21%, displaying over 26% enhancement compared with the reference device without Cu_9S_5 modification. Our research provides an innovative approach to enormously improve the PV

performance of heterojunction PSC devices by applying optically scattering p-type semiconductor SUPs.

Acknowledgments

This work was supported by Natural Science Foundation of Shanghai (Nos. 18ZR1411900, 18ZR1411000) and National Natural Science Foundation of China (No. 11274119). Z B Wang thanks funding support from the 2nd Solar Photovoltaic Academic Research Consortium (SPARC II), the European Regional Development Fund (ERDF) and the Welsh European Funding Office (WEFO).

ORCID iDs

Zengbo Wang https://orcid.org/0000-0002-6813-6751
Xiaohong Chen https://orcid.org/0000-0002-4441-346X
Sumei Huang https://orcid.org/0000-0001-5283-3918

References

[1] Kojima A, Teshima K, Shirai Y and Miyasaka T 2009 Organometal halide perovskites as visible-light sensitizers for photovoltaic cells *J. Am. Chem. Soc.* **131** 6050–1
[2] Kim H-S *et al* 2012 Lead iodide perovskite sensitized all-solid-state submicron thin film mesoscopic solar cell with efficiency exceeding 9% *Sci. Rep.* **2** 591
[3] Lee M M, Teuscher J, Miyasaka T, Murakami T N and Snaith H J 2012 Efficient hybrid solar cells based on meso-superstructured organometal halide perovskites *Science* **338** 643
[4] Chung I, Lee B, He J, Chang R P H and Kanatzidis M G 2012 All-solid-state dye-sensitized solar cells with high efficiency *Nature* **485** 486–9
[5] NREL Transforming ENERGY Best Research-Cell Efficiency Chart (https://www.nrel.gov/pv/cell-efficiency.html)
[6] Jeon N J, Noh J H, Yang W S, Kim Y C, Ryu S, Seo J and Seok S I 2015 Compositional engineering of perovskite materials for high-performance solar cells *Nature* **517** 476–80
[7] Zhang C, Luo Q, Shi J, Yue L, Wang Z, Chen X and Huang S 2017 Efficient perovskite solar cells by combination use of Au nanoparticles and insulating metal oxide *Nanoscale* **9** 2852–64
[8] Luo Q, Zhang C, Deng X, Zhu H, Li Z, Wang Z, Chen X and Huang S 2017 Plasmonic effects of metallic nanoparticles on enhancing performance of perovskite solar cells *ACS Appl. Mater. Interfaces* **9** 34821–32
[9] Tavakoli M M, Saliba M, Yadav P, Holzhey P, Hagfeldt A, Zakeeruddin S M and Grätzel M 2018 Synergistic crystal and interface engineering for efficient and stable perovskite photovoltaics *Adv. Energy Mater.* **9** 1802646
[10] Boyd C C, Cheacharoen R, Leijtens T and McGehee M D 2018 Understanding degradation mechanisms and improving stability of perovskite photovoltaics *Chem. Rev.* **119** 3418–51
[11] Jeon N J, Noh J H, Kim Y C, Yang W S, Ryu S and Seok S I 2014 Solvent engineering for high-performance inorganic-organic hybrid perovskite solar cells *Nat. Mater.* **13** 897–903
[12] Bi D *et al* 2018 Multifunctional molecular modulators for perovskite solar cells with over 20% efficiency and high operational stability *Nat. Commun.* **9** 4482
[13] Choi H, Mai C-K, Kim H-B, Jeong J, Song S, Bazan G C, Kim J Y and Heeger A J 2015 Conjugated polyelectrolyte hole transport layer for inverted-type perovskite solar cells *Nat. Commun.* **6** 348
[14] Liu Y *et al* 2015 A dopant-free organic hole transport material for efficient planar heterojunction perovskite solar cells *J. Mater. Chem.* A **3** 11940–7
[15] Wang S, Yuan W and Meng Y S 2015 Spectrum-dependent Spiro-OMeTAD oxidization mechanism in perovskite solar cells *ACS Appl. Mater. Interfaces* **7** 24791–8
[16] Leijtens T, Lim J, Teuscher J, Park T and Snaith H J 2013 Charge density dependent mobility of organic hole-transporters and mesoporous TiO_2 determined by transient mobility spectroscopy: implications to dye-sensitized and organic solar cells *Adv. Mater.* **25** 3227–33
[17] Bach U, Lupo D, Comte P, Moser J E, Weissörtel F, Salbeck J, Spreitzer H and Grätzel M 1998 Solid-state dye-sensitized mesoporous TiO_2 solar cells with high photon-to-electron conversion efficiencies *Nature* **395** 583–5
[18] Snaith H J and Grätzel M 2006 Enhanced charge mobility in a molecular hole transporter via addition of redox inactive ionic dopant: implication to dye-sensitized solar cells *Appl. Phy. Lett.* **89** 262114
[19] Wang S, Sina M, Parikh P, Uekert T, Shahbazian B, Devaraj A and Meng Y S 2016 Role of 4-tert-butylpyridine as a hole transport layer morphological controller in perovskite solar cells *Nano Lett.* **16** 5594–600
[20] Chen D-Y, Tseng W-H, Liang S-P, Wu C-I, Hsu C-W, Chi Y, Hung W-Y and Chou P-T 2012 Application of F_4TCNQ doped spiro-MeOTAD in high performance solid state dye sensitized solar cells *Phys. Chem. Chem. Phys.* **14** 11689–94
[21] Burschka J, Kessler F, Nazeeruddin M K and Grätzel M 2013 Co (III) complexes as p-dopants in solid-state dye-sensitized solar cells *Chem. Mater.* **25** 2986–90
[22] Comin A and Manna L 2014 New materials for tunable plasmonic colloidal nanocrystals *Chem. Soc. Rev.* **43** 3957–75
[23] Itzhak A *et al* 2018 Digenite (Cu_9S_5) layered p-type semiconductor grown by reactive annealing of copper *Chem. Mater.* **30** 2379–88
[24] Zhou M, Tian M and Li C 2016 Copper-based nanomaterials for cancer imaging and therapy *Bioconjugate Chem.* **27** 1188–99
[25] Wang S *et al* 2015 Plasmonic copper sulfide nanocrystals exhibiting near-infrared photothermal and photodynamic therapeutic effects *ACS Nano* **9** 1788–800
[26] Ornelas-Acosta R E, Shaji S, Avellaneda D, Castillo G A, Das Roy T K and Krishnan B 2015 Thin films of copper antimony sulfide: a photovoltaic absorber material *Mater. Res. Bull.* **61** 215–25
[27] Zhang M-J, Lin Q, Yang X, Mei Z, Liang J, Lin Y and Pan F 2016 Novel p-type conductive semiconductor nanocrystalline film as the back electrode for high-performance thin film solar cells *Nano Lett.* **16** 1218–23
[28] Lei H *et al* 2017 Incorporation of high-mobility and room-temperature-deposited Cu_xS as a hole transport layer for efficient and stable organo-lead halide perovskite solar cells *Solar RRL* **1** 1700038
[29] Han D, Wu C, Zhang Q, Wei S, Qi X, Zhao Y, Chen Y, Chen Y, Xiao L and Zhao Z 2018 Solution-processed cu_9s_5 as a hole transport layer for efficient and stable perovskite solar cells *ACS Appl. Mater. Interfaces* **10** 31535–40
[30] Lei H, Fang G, Cheng F, Ke W, Qin P, Song Z, Zheng Q, Fan X, Huang H and Zhao X 2014 Enhanced efficiency in organic solar cells via *in situ* fabricated p-type copper sulfide as the hole transporting layer *Sol. Energy Mater. Sol. Cells* **128** 77–84
[31] Jang Y H, Jang Y J, Kim S, Quan L N, Chung K and Kim D H 2016 Plasmonic solar cells: from rational design to mechanism overview *Chem. Rev.* **116** 14982–5034

[32] Cushing S K, Li J, Meng F, Senty T R, Suri S, Zhi M, Li M, Bristow A D and Wu N 2012 Photocatalytic activity enhanced by plasmonic resonant energy transfer from metal to semiconductor *J. Am. Chem. Soc.* **134** 15033–41

[33] Carretero-Palacios S, Jiménez-Solano A and Míguez H 2016 Plasmonic nanoparticles as light-harvesting enhancers in perovskite solar cells: a user's guide *ACS Energy Lett.* **1** 323–31

[34] Kakavelakis G, Petridis K and Kymakis E 2017 Recent advances in plasmonic metal and rare-earth-element upconversion nanoparticle doped perovskite solar cells *J. Mater. Chem.* A **5** 21604–24

[35] Zhou D, Liu D, Jin J, Chen X, Xu W, Yin Z, Pan G, Li D and Song H 2017 Semiconductor plasmon-sensitized broadband upconversion and its enhancement effect on the power conversion efficiency of perovskite solar cells *J. Mater. Chem.* A **5** 16559–67

[36] Liu L, Zhong H, Bai Z, Zhang T, Fu W, Shi L, Xie H, Deng L and Zou B 2013 Controllable transformation from rhombohedral $Cu_{1.8}S$ nanocrystals to hexagonal CuS clusters: phase- and composition-dependent plasmonic properties *Chem. Mater.* **25** 4828–34

[37] Stöber W, Fink A and Bohn E 1968 Controlled growth of monodisperse silica spheres in the micron size range *J. Colloid Interface Sci.* **26** 62–9

[38] Zhang C, Luo Q, Deng X, Zheng J, Ou-Yang W, Chen X and Huang S 2017 Enhanced efficiency and stability of carbon based perovskite solar cells using terephthalic acid additive *Electrochim. Acta* **258** 1262–72

[39] Luo Y, Chen X, Zhang C, Li J, Shi J, Sun Z, Wang Z and Huang S 2015 AgAl alloy electrode for efficient perovskite solar cells *RSC Adv.* **5** 56037–44

[40] Jiang Z, Chen X, Lin X, Jia X, Wang J, Pan L, Huang S, Zhu F and Sun Z 2016 Amazing stable open-circuit voltage in perovskite solar cells using AgAl alloy electrode *Sol. Energy Mater. Sol. Cells* **146** 35–43

[41] Liu M, Jia M, Pan H, Li L, Chang M, Ren H, Argoul F, Zhang S and Xu J 2014 Instrument response standard in time-resolved fluorescence spectroscopy at visible wavelength: quenched fluorescein sodium *Appl. Spectrosc.* **68** 577–83

[42] Lai C-W, Wang Y-H, Lai C-H, Yang M-J, Chen C-Y, Chou P-T, Chan C-S, Chi Y, Chen Y-C and Hsiao J-K 2008 Iridium-complex-functionalized Fe_3O_4/SiO_2 Core/shell nanoparticles: a facile three-in-one system in magnetic resonance imaging, luminescence imaging, and photodynamic therapy *Small* **4** 218–24

[43] Choi H, Lee J-P, Ko S-J, Jung J-W, Park H, Yoo S, Park O, Jeong J-R, Park S and Kim J Y 2013 Multipositional silica-coated silver nanoparticles for high-performance polymer solar cells *Nano Lett.* **13** 2204–8

[44] Jain P K and El-Sayed M A 2008 Noble metal nanoparticle pairs: effect of medium for enhanced nanosensing *Nano Lett.* **8** 4347–52

[45] Zhao Y, Pan H, Lou Y, Qiu X, Zhu J and Burda C 2009 Plasmonic $Cu_{2-x}S$ nanocrystals: optical and structural properties of copper-deficient copper(I) sulfides *J. Am. Chem. Soc.* **131** 4253–61

[46] Pysch D, Mette A and Glunz S W 2007 A review and comparison of different methods to determine the series resistance of solar cells *Sol. Energy Mater. Sol. Cells* **91** 1698–706

[47] Lin Z, Chang J, Zhang C, Zhang J, Wu J and Hao Y 2016 Low temperature aqueous solution-processed Li doped ZnO buffer layers for high performance inverted organic solar cells *J. Mater. Chem.* C **4** 6169–75

[48] Wolfram H and Wriedt T 2012 *The Mie Theory Basics and Applications* (Berlin: Springer)

[49] Fan W, Yan B, Wang Z and Wu L 2016 Three-dimensional all-dielectric metamaterial solid immersion lens for subwavelength imaging at visible frequencies *Sci. Adv.* **2** e1600901

[50] Johnson P B and Christy R W 1972 Optical constants of the noble metals *Phys. Rev.* B **6** 4370–9

[51] Palik. E D and Ghosh. G 1999 *Electronic Handbook of Optical Constants of Solids; Sci Vision* (New York: Academic)

[52] Ball J M *et al* 2015 Optical properties and limiting photocurrent of thin-film perovskite solar cells *Energy Environ. Sci.* **8** 602–9

[53] Wintzheimer S, Granath T, Oppmann M, Kister T, Thai T, Kraus T, Vogel N and Mandel K 2018 Supraparticles: functionality from Uniform Structural Motifs *ACS Nano* **12** 5093–120

[54] Mokkapati S, Beck F J, Waele R D, Polman A and Catchpole K R 2011 Resonant nano-antennas for light trapping in plasmonic solar cells *J. Phys. D: Appl. Phys.* **44** 185101

[55] Zhu G, Lin T, Lü X, Zhao W, Yang C, Wang Z, Yin H, Liu Z, Huang F and Lin J 2013 Black brookite titania with high solar absorption and excellent photocatalytic performance *J. Mater. Chem.* A **1** 9650–3

[56] Zuo L, Gu Z, Ye T, Fu W, Wu G, Li H and Chen H 2015 Enhanced photovoltaic performance of $CH_3NH_3PbI_3$ perovskite solar cells through interfacial engineering using self-assembling monolayer *J. Am. Chem. Soc.* **137** 2674–9

[57] Heo J H, Han H J, Kim D, Ahn T K and Im S H 2015 Hysteresis-less inverted $CH_3NH_3PbI_3$ planar perovskite hybrid solar cells with 18.1% power conversion efficiency *Energy Environ. Sci.* **8** 1602–8

[58] Hou X, Zhou J, Huang S, Ou-Yang W, Pan L and Chen X 2017 Efficient quasi-mesoscopic perovskite solar cells using Li-doped hierarchical TiO_2 as scaffold of scattered distribution *Chem. Eng. J.* **330** 947–55

[59] Chang J, Lin Z, Zhu H, Isikgor F H, Xu Q-H, Zhang C, Hao Y and Ouyang J 2016 Enhancing the photovoltaic performance of planar heterojunction perovskite solar cells by doping the perovskite layer with alkali metal ions *J. Mater. Chem.* A **4** 16546–52

[60] Gonzalez-Carrero S, Espallargas G M, Galian R E and Pérez-Prieto J 2015 Blue-luminescent organic lead bromide perovskites: highly dispersible and photostable materials *J. Mater. Chem.* A **3** 14039–45

[61] Lin K-C, Wang L, Doane T, Kovalsky A, Pejic S and Burda C 2014 Combination of optical and electrical loss analyses for a Si-phthalocyanine dye-sensitized solar cell *J. Phys. Chem.* B **118** 14027–36

[62] Li Z, Kolodziej C, McCleese C, Wang L, Kovalsky A, Samia A C, Zhao Y and Burda C 2019 Effect of chloride substitution on interfacial charge transfer processes in $MAPbI_3$ perovskite thin film solar cells: planar versus mesoporous *Nanoscale Adv.* **1** 827–33